

6-1-2012

Structural Characterization of Zn(II)-, Co(II)-, and Mn(II)-loaded Forms of the argE-encoded N-acetyl-L-ornithine Deacetylase from *Escherichia coli*

Ye Tao

University of Georgia

Jacob E. Shokes

University of Georgia

Wade C. McGregor

Arizona State University

Robert A. Scott

University of Georgia

Richard C. Holz

Marquette University

Accepted version. *Journal of Inorganic Biochemistry*, Vol. 111 (June 2012): 157-163. DOI. © 2012

Published by Elsevier B.V. Used with permission.

Richard C. Holz was affiliated with Loyola University-Chicago at the time of publication.

Marquette University

e-Publications@Marquette

Chemistry Faculty Research and Publications/College of Arts and Sciences

This paper is NOT THE PUBLISHED VERSION; but the author's final, peer-reviewed manuscript. The published version may be accessed by following the link in the citation below.

Journal of Inorganic Biochemistry, Vol. 111 (June 2012): 157-163. [DOI](#). This article is © Elsevier and permission has been granted for this version to appear in [e-Publications@Marquette](#). Elsevier does not grant permission for this article to be further copied/distributed or hosted elsewhere without the express permission from Elsevier.

Structural characterization of Zn(II)-, Co(II)-, and Mn(II)-loaded forms of the argE-encoded *N*-acetyl-L-ornithine deacetylase from *Escherichia coli*☆☆☆☆

Ye Tao

University of Georgia, United States

Jacob E. Shokes

University of Georgia, United States

Wade C. McGregor

Arizona State University, United States

Robert A. Scott

University of Georgia, United States

Richard C. Holz

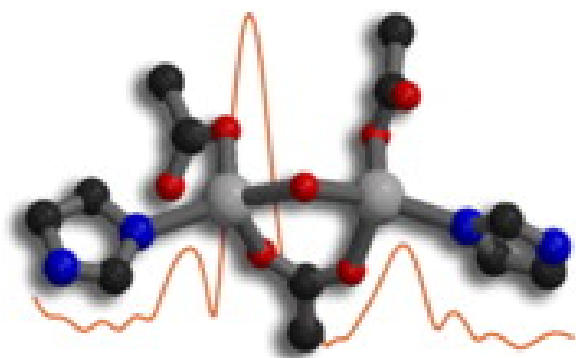
Loyola University Chicago, United States

Abstract

The Zn, Co, and Mn K-edge [extended X-ray absorption fine structure](#) (EXAFS) [spectra](#) of the *N*-acetyl-L-ornithine deacetylase (ArgE) from [Escherichia coli](#), loaded with one or two equivalents of divalent [metal](#) ions (*i.e.*, [Zn(II)_(ArgE)], [Zn(II)Zn(II)(ArgE)], [Co(II)_(ArgE)], [Co(II)Co(II)(ArgE)], [Mn(II)_(ArgE)], and [Mn(II)Mn(II)(ArgE)]), were recorded. The Fourier transformed data (FT) for [Zn(II)_(ArgE)], [Zn(II)Zn(II)(ArgE)], [Co(II)_(ArgE)] and [Co(II)Co(II)(ArgE)] are dominated by a peak at 2.05 Å, that can be fit assuming five or six [light atom](#) (N,O) scatterers. Inclusion of multiple-scattering contributions from the outer-shell atoms of a histidine-imidazole ring resulted in reasonable [Debye–Waller factors](#) for these contributions and a slight [reduction](#) in the [goodness-of-fit](#) value (χ^2). Furthermore, the data best fit a model that included a M–M vector at 3.3 and 3.4 Å for Zn(II) and Co(II), respectively, suggesting the formation of a dinuclear site. Multiple scattering contributions from the outer-shell atoms of a histidine-imidazole rings are observed at ~ 3 and 4 Å for Zn(II)- and Co(II)-loaded ArgE suggesting at least one [histidine ligand](#) at each metal [binding site](#). Likewise, EXAFS data for Mn(II)-loaded ArgE are dominated by a peak at 2.19 Å that was best fit assuming six light atom (N,O) scatterers. Due to poor [signal to noise ratios](#) for the Mn EXAFS spectra, no Mn–Mn vector could be modeled. Peak intensities for [M(II)_(ArgE)] vs. [M(II)M(II)(ArgE)] suggest the Zn(II), Co(II), and Mn(II) bind to ArgE in a cooperative manner. Since no structural data has been reported for any ArgE enzyme, the EXAFS data reported herein represent the first structural glimpse for ArgE enzymes. These data also provide a structural foundation for the future design of small [molecules](#) that function as inhibitors of ArgE and may potentially function as a new class of [antibiotics](#).

Graphical abstract

The Zn, Co, and Mn K-edge EXAFS spectra of *N*-acetyl-L-ornithine deacetylase (ArgE) from *E. coli* are presented. The Fourier transformed data for Zn(II) and Co(II)-loaded ArgE indicate five or six N,O scatterers at 2.05 Å and a M-M vector at ~ 3.4 Å suggesting the formation of a dinuclear site.



Highlights

► The Zn, Co, and Mn K-edge EXAFS spectra of ArgE. ► EXAFS data for Zn(II) and Co(II) ArgE exhibit a peak at 2.05 Å, indicating five or six N,O scatterers. ► Inclusion of a M-M vector 3.4 Å for Zn(II) or Co(II) ArgE suggests the formation of a dinuclear site. ► These data provide a structural base for the future design of small molecule inhibitors of ArgE.

Keywords

EXAFS, ArgE, Hydrolases, Deacetylases, Zinc

1. Introduction

The emergence of [antibiotic](#) resistant bacterial infections has created a significant and growing medical problem in the United States and throughout the world [1], [2], [3], [4], [5]. Currently available antibiotics work on relatively few targets through mechanisms such as inhibiting [protein](#) or cell wall synthesis [6], [7], [8], [9].

Therefore, there is an urgent need to identify novel antibacterial targets and discover small [molecule](#) inhibitors that can function as antimicrobial agents [\[10\]](#). Based on [bacterial genetic](#) information, the [arginine biosynthetic pathway](#) offers several [potential](#) antibacterial enzyme targets, some of which have yet to be explored [\[11\]](#), [\[12\]](#), [\[13\]](#). [Prokaryotes](#) synthesize [arginine](#) through a series of eight enzymatically-catalyzed reactions that differ from those of [eukaryotes](#) by two key steps ([Fig. 1](#)): i) [acetylation](#) of [glutamate](#) (Step 1) and ii) the subsequent [deacetylation](#) of the arginine precursor N^α -acetyl-L-ornithine (L-NAO) by the *argE*-encoded N^α -acetyl-L-ornithine deacetylase (ArgE) (Step 5) [\[14\]](#), [\[15\]](#), [\[16\]](#). The arginine biosynthetic pathway is found in all Gram-negative and most Gram-positive [bacteria](#) including but not limited to [Enterobacteriaceae](#), [Haemophilus](#), [Vibrionaceae](#), [Corynebacterium](#), [Campylobacter](#), [Yersinia pestis](#), [Vibrio cholerae](#), [Bacillus anthracis](#), [Escherichia coli](#) O157:H7, [Shigella flexneri](#), [Shigella typhimurium](#), and [Neisseria gonorrhoeae](#) [\[13\]](#), [\[14\]](#), [\[17\]](#), [\[18\]](#), [\[19\]](#), [\[20\]](#), [\[21\]](#), [\[22\]](#). With the resurgence of [antibiotic resistance](#) in nearly all of these [bacterial strains](#), the search for new antibiotics that target hereto unexplored enzymes involved in [metabolic](#) processes exclusive to these bacteria is critically important in order to renew our arsenal of antibiotics [\[23\]](#).

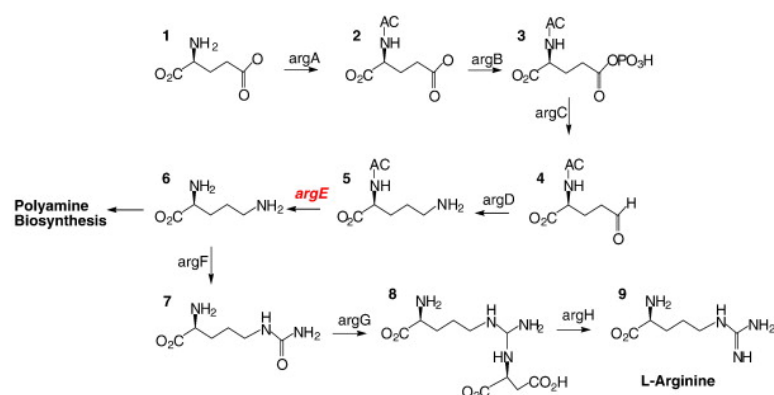


Fig. 1. [Arginine biosynthetic pathway](#) for [prokaryotes](#).

Because [ornithine](#) is required, not only for the synthesis of arginine in bacteria, but also for [polyamines](#) involved in DNA replication and [cell division](#), the L-NAO [deacetylation](#) step is critical for bacterial proliferation [\[24\]](#). Indeed, when Meinel and coworkers transformed an arginine auxotrophic bacterial strain void of L-NAO deacetylase activity with a [plasmid](#) containing *argE*, an Arg⁺ [phenotype](#) resulted [\[25\]](#). However, when the [start codon](#) (ATG) of *argE* in the same plasmid was changed to the Amber [codon](#) (TAG), the resultant plasmid was unable to relieve arginine [auxotrophy](#) in the same cell strain. Therefore, ArgE is required for [cell viability](#). Given the fact that ArgE is only found in prokaryotes and is required for bacterial [cell growth and proliferation](#), it represents an enzymatic target for the [development](#) of a new class of antimicrobial agents [\[24\]](#).

All ArgE enzymes characterized to date require Zn(II) [ions](#) for [enzymatic activity](#) [\[12\]](#), [\[13\]](#), [\[26\]](#) and the [amino acid residues](#) that function as [metal ligands](#) in the [carboxypeptidase](#) from [Pseudomonas](#) sp strain-RS-16 (CPG2), the [aminopeptidase](#) from [Aeromonas proteolytica](#) (AAP), the *dapE*-encoded *N*-succinyl-L, l-diaminopimelic acid desuccinylase from [Haemophilus influenzae](#) (DapE) [\[27\]](#), and the *N*-acetyl-L-citrulline deacetylase (ACD) from [Xanthomonas campestris](#) [\[28\]](#), [\[29\]](#), [\[30\]](#) are strictly conserved in ArgE enzymes [\[12\]](#). CPG2, DapE, and AAP possess a (μ-aquo)(μ-carboxylato)dizinc(II) core with one terminal carboxylate and one [histidine residue](#) at each metal site suggesting a similar [active site](#) exists in ArgE enzymes. The Zn–Zn distance is 3.4, 3.5, and 3.3 Å for DapE, AAP, and CPG₂, respectively, with each [metal ion](#) residing in a distorted tetrahedral coordination geometry. Recently, [kinetic](#) and spectroscopic evidence suggested that the ArgE from [E. coli](#) also contains a dinuclear metalloactive site [\[26\]](#); however, no structural information regarding an ArgE enzyme has yet to be reported. In order to provide evidence for a (μ-aquo)(μ-carboxylato)dizinc(II) core in ArgE enzyme, we have obtained K-edge [extended X-ray absorption fine structure](#) (EXAFS) [spectroscopic data](#) on Zn(II), Co(II), and Mn(II)-loaded ArgE from [E. coli](#). Since [EXAFS](#) is sensitive to heavy [atom](#) scatterers in the second [coordination sphere](#), it is an effective tool for identifying dinuclear metal sites.

2. Materials and methods

2.1. Enzyme expression and purification

All chemicals used in this study were purchased from commercial sources and were of the highest quality available. ArgE from *E. coli* was purified as previously described from a stock culture of *E. coli* BL21 Star™ cells (Invitrogen) hosting the pET-27a(+)*argE* over-expression construct provided by Professor John S. Blanchard [12]. The purified enzyme manifested a single band, on a 12% SDS gel, which corresponds to its calculated M_r of 42,350, by comparison with molecular weight standards purchased from Sigma. It was subsequently concentrated to > 1 mM and stored at 4 °C. Protein concentration was determined using the theoretical value $\epsilon_{280} = 41,250 \text{ M}^{-1} \text{ cm}^{-1}$ [31]. Apo-ArgE samples were exchanged into 50 mM Chelex-100 treated HEPES buffer at pH 7.5 and these samples were incubated anaerobically with MCl_2 (99.999% Strem Chemicals) where M = Zn(II), Co(II) or Mn(II) for ~ 20 min as previously reported [26].

2.2. Enzymatic assay of ArgE

Enzyme kinetic constants were determined in 50 mM Chelex-100 treated sodium phosphate buffer pH 7.5 with L-NAO as the substrate at 25 °C. The rate of NAO deacetylation was monitored as a decrease in absorbance at 214 nm corresponding to the peptide bond ($\Delta\epsilon_{214} = 103 \text{ M}^{-1} \text{ cm}^{-1}$). Catalytic activities were determined within $\pm 10\%$. The specific activity of purified ArgE with L-NAO was typically found to be 2000 units per mg of enzyme, where one unit was defined as the amount of enzyme that releases 1 μmol of ornithine at 25 °C in 60 s. Initial rates were fit directly to the Michaelis–Menten equation to obtain the catalytic constants K_m and k_{cat} .

2.3. X-ray absorption spectroscopy

XAS data were collected at the Stanford Synchrotron Radiation Lightsource (SSRL) with beam current between 80 and 100 mA at 3.0 GeV (Table 1). ArgE EXAFS samples (1 mM), loaded in polycarbonate cuvettes, $24 \times 2 \text{ mm}^2$ with one $24 \times 2 \text{ mm}^2$ face consisting of X-ray transparent Mylar tape, were flash-frozen in $\text{N}_2(\text{l})$ and maintained at 10 K during data collection, using a liquid helium-flow cryostat. XAS fluorescence signals were collected with a 30-element intrinsic Ge solid-state detector and Z-1 fluorescence filters with Soller slits. The edge regions for multiple scans obtained on the same sample were compared to ensure that the sample was not damaged by exposure to X-ray radiation. Harmonic rejection was achieved by setting the cutoff energy of the focusing mirror to an energy between the fundamental and second harmonic (10 keV for Mn, 12 keV for Co and 13 keV for Zn). The energy was calibrated to the inflection points of the edge of the standard Zn, Co, and Mn foil, which were assumed to be at 9660.7, 7709.5, and 6539.0 eV for Zn, Co and Mn, respectively.

Table 1. X-ray absorption data collection.

	Co EXAFS	Zn EXAFS	Mn EXAFS
SR facility	SSRL	SSRL	SSRL
Beamline	9–3	9–3	9–3
Current in storage ring	80–100 mA	80–100 mA	80–100 mA
Monochromator crystal	Si[220]	Si[220]	Si[220]
Detection method	Fluorescence	Fluorescence	Fluorescence
Detector type	Solid state array ^a	Solid state array ^a	Solid state array ^a
Scan length, min	15	15	15
Scans in average	4	4	4 to 7
Temperature, K	10	10	10
Energy standard	Co foil, 1st inflection	Zn foil, 1st inflection	Mn foil, 1st inflection
Energy calibration, eV	7709.5	9660.7	6539.0
E_0 , eV	7715	9670	6545
Pre-edge background			

Energy range, eV	0–7670	0–9625	0–6500
Gaussian center, eV	6930	8638	5898
Gaussian width, eV	750	750	750
Spline background			
Energy range, eV	7715.0–7947.47 (4)	9670.0–9898.63 (4)	6545.00–6778.03 (4)
(polynomial order)	7947.47–8179.95 (4)	9898.63–10127.3 (4)	6778.03–7011.06 (4)
	8179.95–8412.42 (4)	10127.3–10355.9 (4)	7011.06–7244.09 (4)

- a. The 30-element Ge solid-state [X-ray](#) fluorescence detector at SSRL was provided by the NIH Biotechnology Research Resource.

XAS data [reduction](#) was carried out to [extract](#) the EXAFS using EXAFSPAK [software](#) [32] and the theoretical phase and amplitude functions were calculated with FEFF8.0 [33]. The structural model for FEFF calculation was generated based on the (μ -aquo)(μ -carboxylato)dizinc(II) site in the high-resolution crystallographic data for AAP [29]. The Co model for calculation was based on this Zn–Zn model with Co–O distances around 2.05 Å. Because optimization of distances and [Debye–Waller factors](#) for all shells is impossible with such a complicated model, simulations relied on calculated Debye–Waller factors, which required determination of [force constants](#) for all bond–atom pairs. The recursion method incorporated into FEFF was subsequently employed to calculate Debye–Waller factors from force constants. All force constants were calculated via the UFF force field [34], except those for Zn–N_{imid}, Co–N_{imid}, and Mn–N_{imid} as well as C–C and C–N bonds within [imidazole](#) rings. These required DFT calculations based on [vibrational frequencies](#) [35], [36]. For metal–ligand force constant calculations, the values calculated by UFF were halved, as the original values are known to be too large [37]. Multiple scattering analysis was performed as previously described [38]. Both single- and multiple-scattering paths ≤ 4.5 Å from either the Mn(II), Zn(II) or Co(II) atoms were used to identify and quantify imidazole coordination due to [histidine](#). With calculated Debye–Waller factors and the amplitude and phase function of the absorbing and scattering [atom](#), the EXAFS were simulated by allowing only E_0 optimization by EXAFSPAK. The structural model was then manually tuned to optimize the comparison of simulated and observed EXAFS.

3. Results

[Zinc](#), [cobalt](#) and [manganese](#) K-edge [X-ray absorption spectra](#) (XAS) of 1 mM [samples](#) of ArgE with one or two equivalents of added Co(II) (*i.e.* [Co(II)₁(ArgE)] and [Co(II)₂(ArgE)]), Zn(II) (*i.e.* [Zn(II)₁(ArgE)] and [Zn(II)₂(ArgE)]) or Mn(II) (*i.e.* [Mn(II)₁(ArgE)] and [Mn(II)₂(ArgE)]) are shown in [Fig. 2](#), [Fig. 3](#). [Kinetic data](#) were obtained for all [EXAFS](#) samples prior to [data collections](#). k_{cat} and K_m values obtained for ArgE in the presence of one equivalent of Zn(II) towards *N*-acetyl-L-ornithine (NAO) were found to be 1600 s^{-1} and 0.8 mM, respectively, while the addition of a single equivalent of Co(II) provided k_{cat} and K_m values of 3800 s^{-1} and 1.2 mM, respectively. These data are identical to those previously reported [26]. For fully loaded samples (*e.g.* [Co(II)₂(ArgE)], [Zn(II)₂(ArgE)], or [Mn(II)₂(ArgE)]), the EXAFS data reveal an average of both [metal](#) ion environments. For [Co(II)₁(ArgE)] and [Co(II)₂(ArgE)], the [spectra](#) reveal $1s \rightarrow 3d$ pre-edge transitions that occur at 7709 eV with a normalized peak intensity of 0.048 for both ([Fig. 2](#), inset). For both [Mn(II)₁(ArgE)] and [Mn(II)₂(ArgE)], the $1s \rightarrow 3d$ pre-edge transitions reside in nearly the identical [position](#) and exhibit identical shapes but differ in amplitude ([Fig. 3](#), inset). The pre-edge feature (6541 eV) is weak, indicating a high coordination number and symmetric geometry like the Co edge. Since $1s \rightarrow 3d$ pre-edge transitions are Laporte-forbidden in centrosymmetric environments (*e.g.*, octahedral, but not tetrahedral), the intensity of the $1s \rightarrow 3d$ pre-edge transitions is inversely proportional to coordination number (assuming tetrahedral four-coordination). The intensities of the observed transitions for both [Co(II)₁(ArgE)] and [Co(II)₂(ArgE)] and [Mn(II)₁(ArgE)] and [Mn(II)₂(ArgE)] are consistent with, on average, five- or six-coordinate divalent metal sites [39], [40].

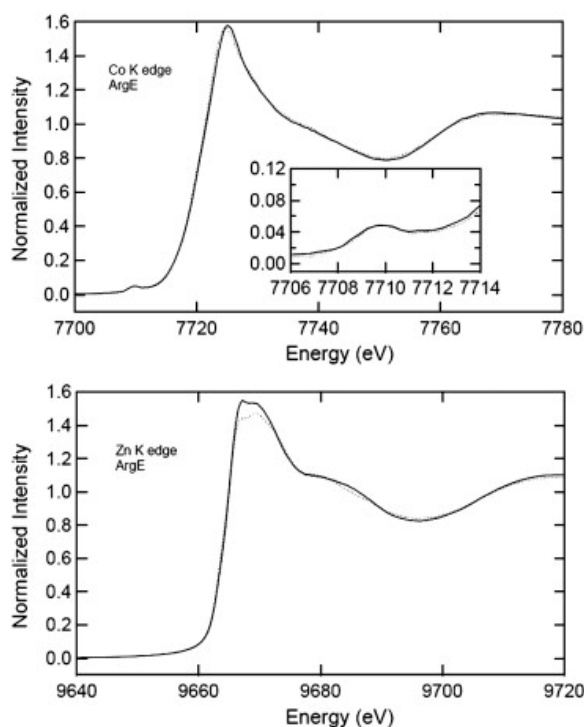


Fig. 2. [X-ray absorption](#) K-edge [spectra](#) for [Co(II)_(ArgE)] (solid) and [Co(II)Co(II)(ArgE)] (dotted) (top) and [Zn(II)_(ArgE)] (solid) and [Zn(II)Zn(II)(ArgE)] (dotted) (bottom). The inset in the top panel highlights the preedge 1s \rightarrow 3d transitions for [Co(II)_(ArgE)] (solid) and [Co(II)Co(II)(ArgE)] (dotted).

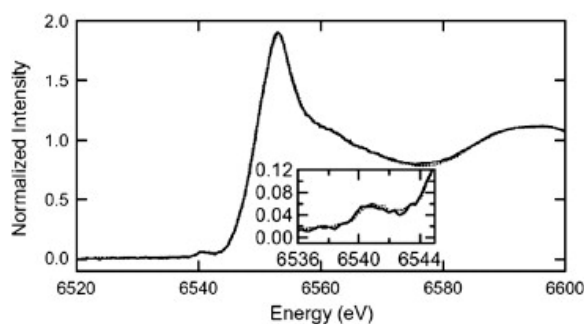


Fig. 3. [X-ray absorption](#) K-edge [spectra](#) for [Mn(II)_(ArgE)] (solid) and [Mn(II)Mn(II)(ArgE)] (dotted). The inset highlights the preedge 1s \rightarrow 3d transitions for [Mn(II)_(ArgE)] (solid) and [Mn(II)Mn(II)(ArgE)] (dotted).

The dominant peak in the Fourier transformed (FT) EXAFS data for [Co(II)_(ArgE)] is centered at 2.11 Å and at 2.10 Å for [Co(II)Co(II)(ArgE)] with amplitude values of 1.78 and 1.61 respectively ([Fig. 4](#); [Table 2](#)). Smaller peaks were also noted at 3.1 Å, 3.4 Å and 4.1 Å with amplitude values of 0.47, 0.14 and 0.32, respectively, for [Co(II)_(ArgE)]. Additional peaks were observed in the FT EXAFS data for [Co(II)Co(II)(ArgE)] at 3.2, 3.4 and 4.1 Å with amplitude values of 0.49, 0.38 and 0.22, respectively. Excellent single-shell fits of [EXAFS spectra](#) for both [Co(II)_(ArgE)] and [Co(II)Co(II)(ArgE)] were obtained with 5 ± 1 N/O scatterers at 2.05 Å. A second shell feature at *ca.* 3.4 Å appears in the [Co(II)Co(II)(ArgE)] EXAFS spectrum. Fits incorporating a Co–Co interaction at 3.4 Å for [Co(II)Co(II)(ArgE)] exhibit reasonable [Debye–Waller factors](#) ([Table 2](#)) and resulted in a significant improvement in [goodness-of-fit](#) values (f'). Failure to incorporate a Co–Co vector in the curve-fitting parameters resulted in a large disagreement between the data and simulation. Therefore, the second-shell FT feature observed at 3.4 Å is consistent with the formation of a dinuclear Co(II) [active site](#) in ArgE.

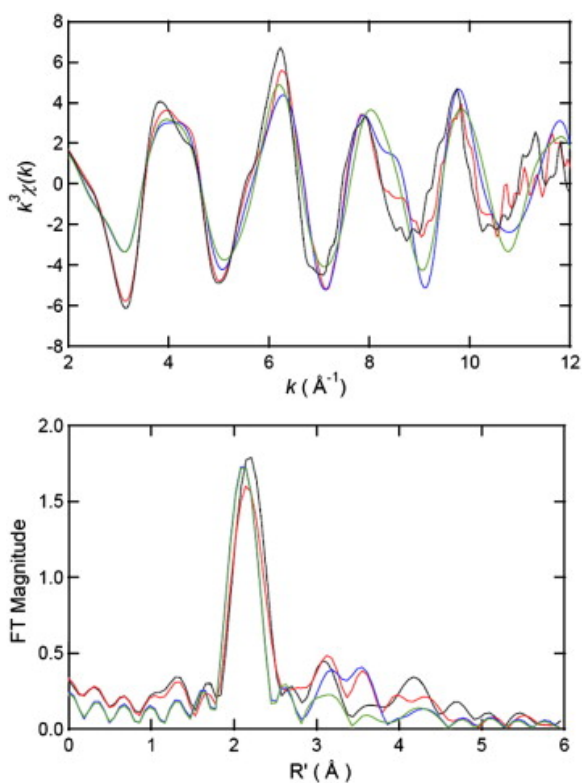


Fig. 4. k^3 -weighted Co EXAFS (top) and Fourier transforms (bottom, over $k = 2\text{--}12 \text{ \AA}^{-1}$) for [Co(II)_(ArgE)] experimental (black) and simulation (green) and for [Co(II)Co(II)(ArgE)] experimental (red) and simulation (blue).

Table 2. Parameters for simulation of Co and Zn ArgE EXAFS_a.

	Shell	R_{as} (Å)	σ_{as}^2 (Å ²)	ΔE_0 (eV)	$f'b$
CoCo(II)_ArgE	Co-N _{His}	2.04	0.0028	10.5	0.100
CRCOB, 2–12 Å ⁻¹	Co-O _{water}	2.05	0.0033		
$\Delta k^3\chi = 11.37$	Co-O _{bridged carboxylate}	2.04	0.0026		
	Co-O _{carboxylate}	2.04	0.0033		
	Co-O _{carboxylate}	2.32	0.0035		
	Co-Co	3.37	0.0042		
ZnZn_ArgE	Zn-N _{His}	2.01	0.0030	8.4	0.136
ZRZOA, 2–12 Å ⁻¹	Zn-O _{water}	2.00	0.0027		
$\Delta k^3\chi = 10.51$	Zn-O _{bridged carboxylate}	2.05	0.0036		
	Zn-O _{carboxylate}	1.99	0.0036		
	Zn-O _{carboxylate}	2.32	0.0039		
	Zn-Zn	3.28	0.0044		

- Here a small part of paths used in simulation are listed. The simulation of Co ArgE includes 54 single and multiple scattering paths while 57 scattering paths in Zn ArgE. R_{as} is the metal-scatterer distance from corresponding molecular model. σ_{as}^2 is a mean square deviation in R_{as} , calculated using UFF model. ΔE_0 is the shift in E_0 for the theoretical scattering functions.
- f' is a normalized error (chi-squared)

Similar to [Co(II)_(ArgE)] and [Co(II)Co(II)(ArgE)], the FT EXAFS spectra of [Zn(II)_(ArgE)] and [Zn(II)Zn(II)(ArgE)] are dominated by a peak at 2.05 Å (Fig. 5; Table 2). However, the amplitude values for this peak are quite similar for [Zn(II)_(ArgE)] and [Zn(II)Zn(II)(ArgE)] (1.56 and 1.50 respectively), suggesting that Zn(II) ions bind to ArgE in a similar manner as Co(II). Additional peaks are observed at 3.0 Å, 3.5 Å and 3.9 Å for [Zn(II)_(ArgE)] and

[Zn(II)Zn(II)(ArgE)], with intensity values of 0.29, 0.33 and 0.26 for [Zn(II)_(ArgE)] and 0.29, 0.40 and 0.26 for [Zn(II)Zn(II)(ArgE)], respectively. Excellent simulations of the observed EXAFS spectra for both [Zn(II)_(ArgE)] and [Zn(II)Zn(II)(ArgE)] were obtained with 5 ± 1 N/O scatterers at 2.00 Å. A second shell feature at *ca.* 3.3 Å is also present in the EXAFS spectrum of [Zn(II)Zn(II)(ArgE)]. Fits incorporating a Zn–Zn interaction at 3.3 Å for [Zn(II)Zn(II)(ArgE)] exhibited reasonable Debye–Waller factors (Table 2) and resulted in a significant improvement in goodness-of-fit values (χ^2). Failure to incorporate a Zn–Zn vector in the curve-fitting parameters resulted in a large disagreement between the data and simulation. Therefore, the second-shell FT feature observed at 3.3 Å is consistent with a dinuclear Zn(II) active site in ArgE.

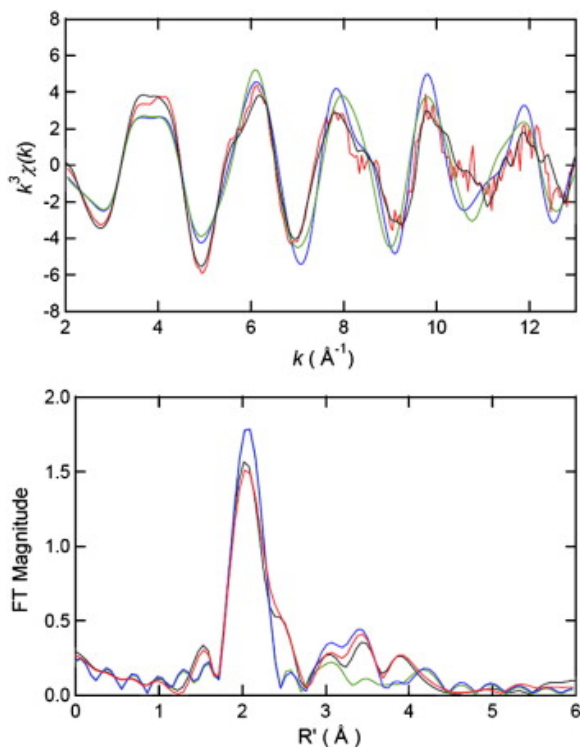


Fig. 5. k^3 -weighted Zn EXAFS (top) and Fourier transforms (bottom, over $k = 2\text{--}12 \text{ Å}^{-1}$) for [Zn(II)_(ArgE)] experimental (black) and simulation (green) and for [Zn(II)Zn(II)(ArgE)] experimental (red) and simulation (blue).

Interestingly, the FT EXAFS spectra of [Mn(II)_(ArgE)] and [Mn(II)Mn(II)(ArgE)] are dominated by a peak at 2.19 Å (Fig. 6; Table 3) which resides at a significantly longer distance than that observed for either Zn(II) or Co(II)-bound ArgE. The amplitudes of this peak for both [Mn(II)_(ArgE)] and [Mn(II)Mn(II)(ArgE)] are quite similar (Fig. 6) suggesting that Mn(II) ions also bind to ArgE in a similar manner as Zn(II) and Co(II). Simulations of the observed EXAFS spectra for both [Mn(II)_(ArgE)] and [Mn(II)Mn(II)(ArgE)] were obtained with 6 ± 1 N/O scatterers at 2.19 Å. However, compared to the EXAFS data obtained for Zn(II) and Co(II)-loaded ArgE, the EXAFS data for Mn(II) are of lower quality making it difficult to identify a possible Mn–Mn interaction or histidine ligation (notice the similar height of FT peaks in the 3–4 Å region and the noise). It should be noted, that there is a visible shoulder at $\sim 4 \text{ Å}^{-1}$ in the EXAFS data for both [Mn(II)_(ArgE)] and [Mn(II)Mn(II)(ArgE)], which suggests the presence of histidine ligands.

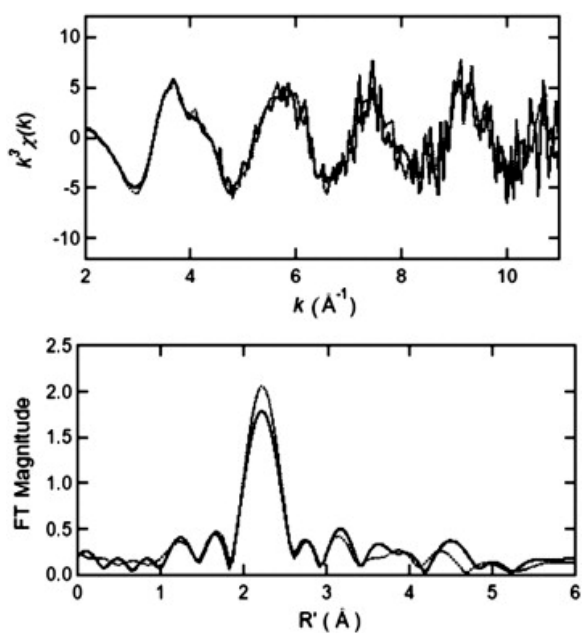


Fig. 6. k^3 -weighted Mn EXAFS (top) and Fourier transforms (bottom, over $k = 2\text{--}12 \text{ \AA}^{-1}$) for [Mn(II)_(ArgE)] (solid) and [Mn(II)Mn(II)(ArgE)] (dotted).

Table 3. Curve fitting results for ArgE Mn K-edge EXAFS_a.

Sample, filename (k range) $\Delta k^3\chi$	Fit	Shell	R_{as} (Å)	σ_{as}^2 (Å ²)	ΔE_0 (eV)	f'
[Mn(II)_(ArgE)] _c	1	Mn–O ₅	2.18	0.0061	1.39	0.229
($k = 2 - 11 \text{ \AA}^{-1}$)	2	Mn–O ₆	2.18	0.0082	1.33	0.248
$\Delta k^3\chi = 14.05$						
[Mn(II)Mn(II)(ArgE)] _c	3	Mn–O ₅	2.18	0.0044	1.75	0.141
($k = 2 - 11 \text{ \AA}^{-1}$)	4	Mn–O ₆	2.18	0.0063	1.65	0.161
$\Delta k^3\chi = 13.89$						

- Shell is the chemical unit defined for the multiple scattering calculation. Subscripts denote the number of scatterers per metal. R_{as} is the metal–scatterer distance. σ_{as}^2 is a mean square deviation in R_{as} . ΔE_0 is the shift in E_0 for the theoretical scattering functions.
- f' is a normalized error (chi-squared):
- The fits for Mn ArgE use the smoothed data.

Inclusion of multiple-scattering contributions from the outer-shell atoms of a histidine-imidazole ring for the FT features observed at ~ 3 and 4 \AA for [Co(II)_(ArgE)], [Co(II)Co(II)(ArgE)], [Zn(II)_(ArgE)], and [Zn(II)Zn(II)(ArgE)], resulted in reasonable Debye–Waller factors for these contributions and a slight reduction in f' (Table 2). These fits are similar to those reported for the FT EXAFS spectra of AAP and DapE [41]. The X-ray crystal structures of AAP and DapE reveal a (μ -aquo)(μ -carboxylato)dizinc(II) active site containing one histidine residue bound to each Zn(II) ion [27], [42]. The amplitude values for the features observed at ~ 3 and 4 \AA are distinct for [Zn(II)_(DapE)] vs. [Zn(II)Zn(II)(DapE)] and [Zn(II)_(AAP)] vs. [Zn(II)Zn(II)(AAP)] [41], but are similar for [Zn(II)_(ArgE)] vs. [Zn(II)Zn(II)(ArgE)] (Fig. 7) suggesting that divalent metal ions bind to ArgE in a positive cooperative manner.

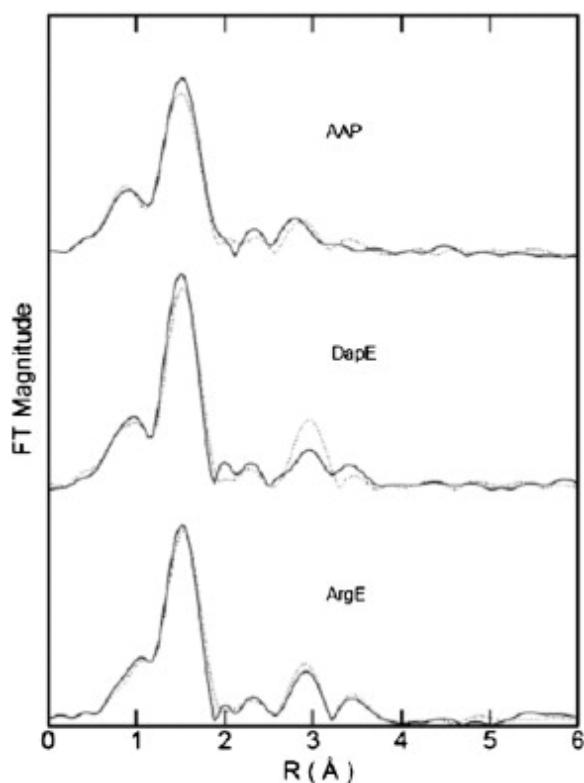


Fig. 7. Non-phase corrected [Fourier transforms](#) over $k = 2\text{--}12 \text{ \AA}^{-1}$ for $[\text{Zn(II)}]_{\text{ArgE}}$ (bottom; solid) and $[\text{Zn(II)Zn(II)}]_{\text{ArgE}}$ (bottom; dotted), for $[\text{Zn(II)}]_{\text{DapE}}$ (middle; solid) and $[\text{Zn(II)Zn(II)}]_{\text{DapE}}$ (middle; dotted) and for $[\text{Zn(II)}]_{\text{AAP}}$ (top; solid) and $[\text{Zn(II)Zn(II)}]_{\text{AAP}}$ (top; dotted).

4. Discussion

The [evolution](#) of bacterial [resistance](#) to [antibiotics](#) poses an imminent health threat to [humans](#). The [arginine biosynthetic pathway](#) offers several [potential](#) anti-bacterial targets that have yet to be explored ([Fig. 1](#)) [[14](#)], [[15](#)], [[25](#)], [[43](#)]. Since ArgE is critical to bacterial [cell survival](#) and proliferation, and no ArgE homolog is produced by humans, this enzyme holds great promise as a new antibiotic target. To date, no [X-ray](#) crystallographic data have been reported for any ArgE enzyme and no catalytically important [amino acid residues](#) have been identified. Therefore, the catalytically competent mono- and di-Zn(II), Co(II) and Mn(II)-loaded forms of ArgE were examined by [extended X-ray absorption fine structure](#) (EXAFS) [spectroscopy](#). EXAFS is particularly well suited to clarify the structures of dinuclear [metalloenzymes](#) since EXAFS data are sensitive to heavy [atom](#) scatterers in the second [coordination sphere](#) providing direct evidence for dinuclear sites, if they exist [[44](#)], [[45](#)].

The EXAFS $1s \rightarrow 3d$ pre-edge transitions observed Co(II)-loaded ArgE at 7709 eV for both the mono- and dinuclear Co(II) ArgE enzymes, are consistent with Co(II) residing in five or six-coordinate geometries [[39](#)], [[40](#)]. These data are in good agreement with previously reported electronic [absorption spectra](#) of Co(II)-loaded ArgE [[26](#)]. For $[\text{Co(II)}]_{\text{ArgE}}$, three distinct peaks at 560, 619 and 705 nm with [molar absorptivities](#) (ϵ) of $\epsilon_{560} = 114 \text{ M}^{-1} \text{ cm}^{-1}$, $\epsilon_{619} = 119 \text{ M}^{-1} \text{ cm}^{-1}$ and $\epsilon_{705} = 52 \text{ M}^{-1} \text{ cm}^{-1}$ were observed. Addition of a second equivalent of Co(II) to $[\text{Co(II)}]_{\text{ArgE}}$ increased the intensity of each of the observed absorption bands providing ϵ values of $\epsilon_{560} = 229 \text{ M}^{-1} \text{ cm}^{-1}$, $\epsilon_{619} = 290 \text{ M}^{-1} \text{ cm}^{-1}$ and $\epsilon_{705} = 121 \text{ M}^{-1} \text{ cm}^{-1}$. These data suggest that both Co(II) [binding sites](#) in ArgE are five coordinate. Similarly, EPR spectra of $[\text{Co(II)}]_{\text{ArgE}}$ and $[\text{Co(II)Co(II)}]_{\text{ArgE}}$ revealed the presence of three [species](#) termed the Rhombic, Axial, and Dicobalt signals [[26](#)]. The predominant signal observed from $[\text{Co(II)}]_{\text{ArgE}}$ is the Rhombic signal, which exhibits high rhombic distortion of the axial [zero-field splitting](#) parameter, suggestive of a highly axially asymmetric [ligand](#) field. The Rhombic signal also exhibits resolved ^{59}Co [hyperfine structure](#), indicative of low strains in the [spin Hamiltonian](#) parameters, *i.e.* of a site with a low degree of conformational freedom. Taken together EXAFS, [UV-vis](#), and EPR data suggest a low symmetry

site, likely five-coordinate, with a geometry constrained by inflexible [protein](#) bound ligands. For [Co(II)Co(II)(ArgE)], a second, broad signal (the Dicobalt signal) is observed and this signal increases in intensity between the addition of one and two equivalents of Co(II); at the same time, both the intensity of the Rhombic signal and the total intensity of the spectrum decrease with added Co(II). The increase in the Dicobalt signal and concomitant decrease in the Rhombic signal are indicative of the formation of a dinuclear center and a consequent change in the electronic structure of the first-Co(II) binding site. These data are also similar to those reported for two dinuclear metallohydrolases from family M28, AAP and DapE [46], [47], [48], [49]. For both AAP and DapE, UV-vis, EPR, and EXAFS data indicate that the first [metal](#) binding site resides in a five-coordinate geometry while the second is either five or six-coordinate.

Similar to Co(II)-loaded ArgE, the EXAFS $1s \rightarrow 3d$ pre-edge transitions observed for Mn(II)-loaded ArgE at 6541 eV for both the mono- and di-nuclear Mn(II) and Co(II) ArgE enzymes are consistent with both Mn(II) sites in ArgE residing in five or six-coordinate geometries (30). These data are consistent with previously reported EPR data on Mn(II)-loaded ArgE where the EPR spectra of [Mn(II)_(ArgE)] and [Mn(II)Mn(II)(ArgE)] are similar except that [Mn(II)Mn(II)(ArgE)] exhibits a more intense six-line pattern centered around 3500 G ($A = 8.8$ mT) and additional features at 1200 and 2100 G [50]. These EPR spectra are characteristic of mononuclear Mn(II) [ions](#) [50]. In addition, no appreciable change in any of the spectra over the [temperature](#) range 4–70 K was observed and no features in the parallel mode spectra were observed that could not be accounted for by transitions due to isolated mononuclear Mn(II). Moreover, the EPR spectrum of [Mn(II)Mn(II)(ArgE)] does not contain a well-resolved 45 G [hyperfine splitting](#), typical of dinuclear Mn(II)–Mn(II) centers when recorded at [pH](#) 7.5, but such a pattern is apparent in the spectrum of [Mn(II)Mn(II)(ArgE)] in 50 mM CAPS [buffer](#) at [pH](#) 10.0 [50]. These data clearly indicate the formation of a dinuclear [active site](#) but only at high [pH](#) values, suggesting coordination of a [hydroxide](#) ion is required to couple the Mn(II) ions. Such [behavior](#) is unique compared to that of [Co(II)Co(II)(ArgE)], which was shown to be coupled by a hydroxide ion at physiological [pH](#) [26].

The phase-corrected FT [EXAFS spectra](#) of [Co(II)_(ArgE)] and [Co(II)Co(II)(ArgE)] are similar to those of Zn(II)-loaded ArgE, which are dominated by a peak at *ca.* 2.05 Å. On the other hand, the phase-corrected FT EXAFS spectra of [Mn(II)_(ArgE)] and [Mn(II)Mn(II)(ArgE)] are dominated by a peak at *ca.* 2.19 Å, which is significantly longer than that observed for either Zn(II) or Co(II). Excellent single-shell fits of these first shell features for [Mn(II)_(ArgE)], [Co(II)_(ArgE)] and [Zn(II)_(ArgE)] were obtained and indicate that 5 or 6 N/O scatterers per Mn(II), Co(II) or Zn(II) ion exists at 2.19, 2.11 or 2.05 Å, respectively (Table 2, Table 3). Similarly, excellent single-shell fits of the first shell features observed in the EXAFS spectra of [Co(II)Co(II)(ArgE)], [Mn(II)Mn(II)(ArgE)], and [Zn(II)Zn(II)(ArgE)] were obtained and also indicate 5 or 6 N/O scatterers per Co(II), Mn(II), or Zn(II) ion at 2.19, 2.19, and 2.05 Å, respectively (Table 2, Table 3). These fits provide the average metal–ligand distances at the first metal site for [Co(II)_(ArgE)], [Mn(II)_(ArgE)], and [Zn(II)_(ArgE)], but are the average metal–ligand distances for both sites in [Co(II)Co(II)(ArgE)], [Mn(II)Mn(II)(ArgE)], and [Zn(II)Zn(II)(ArgE)]. The 0.09 Å difference in the dominant peak [position](#) in the phase-corrected FT spectra for Mn(II)-loaded ArgE vs. Co(II)- or Zn(II)-loaded ArgE, indicates that the Mn(II) bond distances are slightly longer than those observed for either Co(II) or Zn(II). This increase in bond distance likely represents the increased ionic radius for Mn(II) (0.97 Å) vs. Co(II) (0.89 Å) and Zn(II) (0.87 Å) in octahedral geometries [51]. In addition, a higher coordination number and greater static order for Mn(II)-loaded ArgE vs. Co(II)- and Zn(II)-loaded ArgE is consistent with the [thermodynamic](#) data generated from [Arrhenius plots](#) for [Mn(II)_(ArgE)], [Zn(II)_(ArgE)] and [Co(II)_(ArgE)] [26], [50]. More negative [entropy](#) values were observed for [Zn(II)_(ArgE)] and [Co(II)_(ArgE)] (– 106 and – 66.0 J/mol·K, respectively) than for [Mn(II)_(ArgE)] (– 34.5 J/mol·K), suggesting more order is imposed on Zn(II)- and Co(II)-loaded ArgE active sites during [catalysis](#) compared with the Mn(II)-loaded form. Furthermore, the rhombic EPR signal observed for [Mn(II)_(ArgE)] exhibits well-resolved ^{55}Mn hyperfine structure, indicating low strains in the [spin](#) Hamiltonian parameters [50]. Weak ^{59}Co hyperfine structure is also observed for [Co(II)_(ArgE)] suggesting that Co(II) also binds with a somewhat low degree of conformational freedom [26].

The phase corrected FT EXAFS spectra of [Co(II)Co(II)(ArgE)] and [Zn(II)Zn(II)(ArgE)] include a feature at ~ 3.3 Å, which is similar to that observed in the phase corrected FT EXAFS spectra of the crystallographically characterized enzymes [urease](#) [52], AAP, and DapE [41] that contain dinuclear active sites. This feature was modeled as a M–M interaction suggesting each of these enzymes contain a dinuclear active site. Indeed, when a M–M vector is omitted from the EXAFS fits, significant disagreement between the observed data and the simulation occurs. For both [Co(II)Co(II)(ArgE)] and [Zn(II)Zn(II)(ArgE)], excellent simulations of EXAFS spectra were obtained with a M–M distance of 3.40 Å and 3.28 Å, respectively. [Sequence alignment](#) of several ArgE [genes](#) with those of the crystallographically characterized AAP, DapE, and CPG₂ enzymes indicates that all of the amino acids that function as metal ligands in AAP, DapE, and CPG₂ are strictly conserved in ArgEs [12], [27], [53], [54]. The [X-ray crystal structures](#) of CPG₂, DapE, and AAP reveal a (μ -aquo)(μ -carboxylato)dizinc(II) active site with one terminal carboxylate and [histidine](#) residue bound to each [metal ion](#) [27], [28], [29]. Both Zn(II) ions in AAP, DapE, and CPG₂ reside in distorted tetrahedral or pentacoordinate geometries, with Zn–Zn distances of 3.5, 3.4, and 3.3 Å for AAP, DapE, and CPG₂, respectively. EXAFS data obtained for [Zn(II)Zn(II)(AAP)] and [Zn(II)Zn(II)(DapE)] also contain features at 3.27 and 3.39 Å, respectively, that can be modeled as a Zn–Zn vector [41]. Combination of these data, indicates that ArgE enzymes contain a dinuclear Zn(II) active site. In addition, based on the X-ray crystal structures and first shell EXAFS fits for [Zn(II)Zn(II)(AAP)] and [Zn(II)Zn(II)(DapE)] vs. those of Zn(II)-, Co(II)-, and Mn(II)-loaded ArgE, we propose that one carboxylate and one [histidine residue](#) reside at each Zn(II) site in ArgE and that the two Zn(II) ions are bridged by one carboxylate residue and a water molecule (Fig. 8).

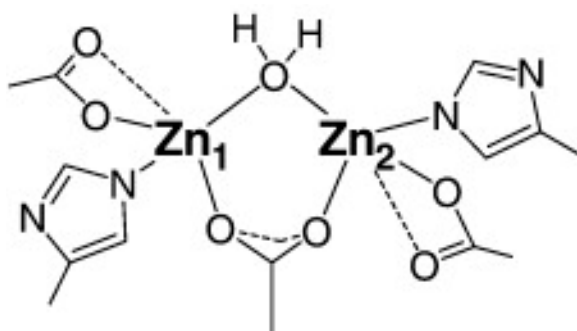


Fig. 8. Proposed [active site](#) of the ArgE from [E. coli](#) based on [EXAFS](#) data.

Interestingly, the phase corrected FT EXAFS spectrum of [Zn(II)](ArgE) could also be simulated with the inclusion of a 3.28 Å Zn–Zn vector. The amplitude of the feature corresponding to the Zn–Zn vector in the phase corrected FT EXAFS spectra of [Zn(II)](ArgE) and [Zn(II)Zn(II)(ArgE)] is striking. For DapE and AAP, the lack of a feature in the 3 to 4 Å for the mono-Zn(II)-loaded form vs. a strong feature in this range for the dinuclear Zn(II) enzymes has been attributed to sequential [metal binding](#) for the dinuclear site. Sequential binding has been verified for DapE as X-ray crystal structures for both the mono- and dinuclear Zn(II) DapE enzymes have been reported [27]. On the other hand, similar amplitudes for the feature in the 3 to 4 Å range for [Zn(II)](ArgE) and [Zn(II)Zn(II)(ArgE)] suggest positive [cooperativity](#) in Zn(II) binding to ArgE. Similarly, the EXAFS features in the 3 to 4 Å range for both Mn(II)- and Co(II)-loaded ArgE also suggest positive cooperativity in divalent metal binding. Taken together, these data suggest that divalent metal ions bind differently to ArgE than AAP or DapE even though the active site ligands appear to be identical [12], [53]. Indeed, electronic absorption and EPR spectra for [Zn(II)Co(II)(ArgE)] vs. [Co(II)Zn(II)(ArgE)] and [Mn(II)Zn(II)(ArgE)] vs. [Zn(II)Mn(II)(ArgE)] are identical, whereas spectral data for [Zn(II)Co(II)(AAP)] and [Co(II)Zn(II)(AAP)] are distinct [47].

In conclusion, ArgE enzymes are potential molecular targets for a novel class of [antibiotics](#). The observation that ArgE is active in the presence of a broad variety of [transition metals](#), including Zn(II), Co(II), or Mn(II), underscores the critical nature of this enzyme to bacterial [cell survival](#) (*i.e.* limiting Zn(II) will not halt ArgE activity because other divalent metal ions can substitute). The EXAFS data reported herein demonstrate that the

ArgE from [E. coli](#) forms a dinuclear metalloactive site in the presence of Zn(II), Co(II), and Mn(II). In addition, multiple scattering contributions from the outer-shell atoms of a histidine-imidazole rings are observed at ~ 3 and 4 Å for Zn(II)- and Co(II)-loaded ArgE suggesting at least one [histidine](#) ligand at each metal binding site. Since no structural data have been reported for any ArgE enzyme, the EXAFS data reported herein represent the structural first glimpse into the active site of ArgE enzymes. Moreover, EXAFS data obtained for Zn(II)-, Co(II)-, and Mn(II)-loaded ArgE indicate that each of these divalent metal ions binds in a positive cooperative manner, in [contrast](#) to the metal binding properties of AAP and DapE [47], [49], [55]. Finally, these data provide a structural foundation for the future design of [small molecules](#) that will function as inhibitors of ArgE and may potentially function as a new class of antibiotics.

References and Notes

- [1] CDC.a. Prevention *MMWR Morb. Mortal. Wkly Rep.*, Vol. 44 (1995), pp. 1-13
- [2] R.A. Howe, K.E. Bowker, T.R. Walsh, T.G. Feest, A.P. MacGowan *Lancet*, 351 (1997), pp. 601-602
- [3] S.B. Levy *Sci. Am.*, 278 (1998), pp. 46-53
- [4] J. Chin *New Sci.*, 152 (1996), pp. 32-35
- [5] C.M. Henery *C&E News* (2000), pp. 41-58
- [6] C. Walsh *Nat. Rev. Microbiol.*, 1 (2003), pp. 65-70
- [7] M. Leeb *Nature*, 431 (2004), pp. 892-893
- [8] M. Schmid *Nat. Biotechnol.*, 24 (2006), pp. 419-420
- [9] D.J. Payne *Science*, 321 (2008), pp. 1644-1645
- [10] C.T. Supuran, A. Scozzafava, B.W. Clare *Med. Res. Rev.*, 22 (2002), pp. 329-372
- [11] N. Glansdorff, Y. Xu V.F. Wendisch (Ed.), *Microbiology Monogr.*, Springer Berlin, Heidelberg (2007), pp. 219-257
- [12] F. Javid-Majd, J.S. Blanchard *Biochemistry*, 39 (2000), pp. 1285-1293
- [13] A.M. Velasco, J.I. Leguina, A. Lazcano *J. Mol. Evol.*, 55 (2002), pp. 445-459
- [14] R. Cunin, N. Glansdorff, A. Pierard, V. Stalon *Microbiol. Rev.*, 50 (1986), pp. 314-352
- [15] R.H. Davis *Microbiol. Rev.*, 50 (1986), pp. 280-313
- [16] R. Ledwidge, J.S. Blanchard *Biochemistry*, 38 (1999), pp. 3019-3024
- [17] V.A. Sakanian, A.S. Ovespian, I.L. Mett, A.V. Kochikian, P.K. Petrosian *Genetika*, 26 (1990), pp. 1915-1925
- [18] Y. Xu, Z. Liang, C. Legrain, H.J. Ruger, N. Glansdorff *J. Bacteriol.*, 182 (2000), pp. 1609-1615
- [19] V. Sakanyan, P. Petrosyan, M. Lecocq, A. Boyen, C. Legrain, M. Demarez, J.N. Hallet, N. Glansdorff *Microbiology*, 142 (1996), pp. 99-108
- [20] E.K. Hani, D. Ng, V.L. Chan *Can. J. Microbiol.*, 45 (1999), pp. 959-969
- [21] V.E. Valentsev, V.I. Krupenina, B.N. Mishan'kin *Zh. Mikrobiol. Epidemiol. Immunobiol.*, 5 (1995), pp. 48-51
- [22] F.J. Picard, J.R. Dillon *J. Bacteriol.*, 171 (1989), pp. 1644-1651
- [23] J.R. Miller, S. Dunham, I. Mochalkin, C. Banotai, M. Bowman, S. Buist, B. Dunkle, D. Hanna, H.J. Harwood, M.D. Huband, A. Karnovsky, M. Kuhn, C. Limberakis, J.Y. Liu, S. Mehrens, W.T. Mueller, L. Narasimhan, A. Ogden, J. Ohren, J.V.N.V. Prasad, J.A. Shelly, L. Skerlos, M. Sulavik, V.H. Thomas, S. VanderRoest, L. Wang, Z. Wang, A. Whitton, T. Zhu, C.K. Stover *Proc. Natl. Acad. Sci. U. S. A.*, 106 (2009), pp. 1737-1742
- [24] J.-M. Girondeau, C. Agouridas, M. Masson, P.R., F. LeGoffic *J. Med. Chem.*, 29 (1986), pp. 1023-1030
- [25] T. Meinnel, E. Schmitt, Y. Mechulam, S. Blanquet *J. Bacteriol.*, 174 (1992), pp. 2323-2331
- [26] W. McGregor, S.I. Swierczek, B. Bennett, R.C. Holz *J. Am. Chem. Soc.*, 127 (2005), pp. 14100-14107
- [27] B.P. Nocek, D.M. Gillner, Y. Fan, R.C. Holz, A. Joachimiak *J. Mol. Biol.*, 397 (2010), pp. 617-626
- [28] S. Rowsell, R.A. Pauptit, A.D. Tucker, R.G. Melton, D.M. Blow, P. Brick *Structure*, 5 (1997), pp. 337-347
- [29] B. Chevrier, C. Schalk, H. D'Orchymont, J.-M. Rondeau, D. Moras, C. Tarnus *Structure*, 2 (1994), pp. 283-291
- [30] D. Shi, X. Yu, L. Roth, M. Tuchman, N.M. Allewell *Biophys. Chem.*, 126 (2007), pp. 86-93
- [31] S.C. Gill, P.H. von Hippel *Anal. Biochem.*, 182 (1989), pp. 319-326
- [32] G.N. George, R.M. Garrett, R.C. Prince, K.V. Rajagopalan *J. Am. Chem. Soc.*, 118 (1996), pp. 8588-8592
- [33] J.J. Rehr, J. Mustre de Leon, S.I. Zabinsky, R.C. Albers *J. Am. Chem. Soc.*, 113 (1991), pp. 5135-5140
- [34] A.C. Rappe, C.J., K.S. Colwell, W.A. Goddard III, W.M. Skiff *J. Am. Chem. Soc.*, 114 (1992), pp. 10024-10035

- [35] G.C. Ferreira, R. Franco, A. Mangravita, G.N. George *Biochemistry*, 41 (2002), pp. 4809-4818
- [36] A.V. Poiarkova, J.J. *Phys. Rev. B*, 59 (1999), p. 948
- [37] A.V. Poiarkova, dissertation, University of Washington, 1999.
- [38] N.J. Cosper, C.M.V. Stalhandske, R.E. Saari, R.P. Hausinger, R.A. Scott *J. Biol. Inorg. Chem.*, 4 (1999), pp. 122-129
- [39] M.D. Wirt, I. Sagi, E. Chen, S.M. Frisbis, R. Lee, M.R. Chance *J. Am. Chem. Soc.*, 113 (1991), pp. 5299-5304
- [40] J.H. Zhang, D.M. Kurtz, M.J. Maroney, J.P. Whitehead vol. *Inorg. Chem.* (1991), pp. 1359-1366
- [41] N.J. Cosper, D.L. Bienvenue, J. Shokes, D.M. Gilner, T. Tsukamoto, R. Scott*, R.C. Holz* *J. Am. Chem. Soc.*, 125 (2004), pp. 14654-14655
- [42] W. Desmarais, L.D. Bienvenue, K.P. Bzymek, R.C. Holz, A.G. Petsko, D. Ringe *Structure* (2002), pp. 1063-1072
- [43] N. Glansdorff **Biosynthesis of arginine and polyamines** F.C. Neidhardt, R. Curtiss III, J.L. Ingraham, E.C.C. Lin, K.B. Low, B. Magasanik, W.S. Reznikoff, M. Riley, M. Schaechter, H.E. Umbarger (Eds.), *Escherichia coli and Salmonella: Cellular and Molecular Biology*, 2nd ed., vol. 1, *American Society for Microbiology*, Washington, D.C. (1996), pp. 408-433
- [44] R.A. Scott *Methods Enzymol.*, 117 (1985), pp. 414-458
- [45] B.K. Teo *Journal* (1981) Pages.
- [46] B. Bennett, R.C. Holz *J. Am. Chem. Soc.*, 119 (1997), pp. 1923-1933
- [47] B. Bennett, R.C. Holz *Biochemistry*, 36 (1997), pp. 9837-9846
- [48] J.M. Prescott, F.W. Wagner, B. Holmquist, B.L. Vallee *Biochemistry*, 24 (1985), pp. 5350-5356
- [49] D.L. Bienvenue, D.M. Gilner, R.S. Davis, B. Bennett, R.C. Holz *Biochemistry*, 42 (2003), pp. 10756-10763
- [50] W.C. McGregor, S.I. Swierczek, B. Bennett, R.C. Holz *J. Biol. Inorg. Chem.*, 12 (2007), pp. 603-613
- [51] F.A. Cotton, G. Wilkinson, C.A. Murillo, M. *Adv. Inorg. Chem.* (1999)
- [52] Shengke Wang, Mann H. Lee, Robert P. Hausinger, Patrick A. Clark, Dean E. Wilcox, Robert A. Scott *Inorg. Chem.*, 33 (8) (1994), pp. 1589-1593
- [53] H.S. Speno, R. Luthi-Carter, W.L. Macias, S.L. Valentine, A.R.T. Joshi, J.T. Coyle *Mol. Pharmacol.*, 55 (1999), pp. 179-185
- [54] D.M. Gillner, D.L. Bienvenue, B.P. Nocek, A. Joachimiak, V. Zachary, B. Bennett, R.C. Holz *J. Biol. Inorg. Chem.*, 14 (2009), pp. 1-10
- [55] J.M. Prescott, F.W. Wagner, B. Holmquist, B.L. Vallee *Biochem. Biophys. Res. Commun.*, 114 (1983), pp. 646-652

☆ Contribution from the Department of Chemistry, Loyola University Chicago, 1068 W. Sheridan Rd., Chicago, IL 60626, the Department of Chemistry and Biochemistry & Molecular Biology, University of Georgia, Athens, Georgia 30602-2556, and the Department of Applied Sciences and Mathematics, College of Technology and Innovation, Arizona State University, Mesa, AZ 85212.

☆☆ This work was supported by the National Institutes of Health ([R15 AI085559-01A1](#), RCH) while the XAS work in the R.A. Scott laboratory was also supported by the National Institutes of Health ([GM042025](#), RAS).